

UNCLASSIFIED

Defense Technical Information Center
Compilation Part Notice

ADP011017

TITLE: Nanoparticle Assembly via Hydrogen-Bonding: IRS, TEM and AFM Characterizations

DISTRIBUTION: Approved for public release, distribution unlimited

This paper is part of the following report:

TITLE: Materials Research Society Symposium Proceedings Volume 635.
Anisotropic Nanoparticles - Synthesis, Characterization and Applications

To order the complete compilation report, use: ADA395000

The component part is provided here to allow users access to individually authored sections of proceedings, annals, symposia, etc. However, the component should be considered within the context of the overall compilation report and not as a stand-alone technical report.

The following component part numbers comprise the compilation report:

ADP011010 thru ADP011040

UNCLASSIFIED

Nanoparticle Assembly via Hydrogen-Bonding: IRS, TEM and AFM Characterizations

Li Han, Mathew M. Maye, Chuan-Jian Zhong

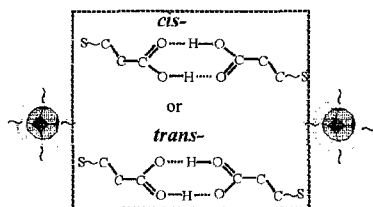
Department of Chemistry, State University of New York at Binghamton, Binghamton, New York 13902.

ABSTRACT

This paper reports results of the characterizations of nanoparticle assembly formed via spontaneous core-shell and shell-shell reactivities at thiolate-capped gold nanoparticles. Gold nanoparticles of two different core sizes and thiols with carboxylic acid terminals are exploited as a model system. The reactivities involve covalent Au-thiolate bonding and non-covalent hydrogen-bonding with anisotropic linking character. We employed infrared reflection spectroscopy (IRS), atomic force microscopy (AFM) and transmission electron microscopy (TEM) for the characterizations. While IRS provides structural assessment, TEM and AFM imaging measurements probe the morphological properties.

INTRODUCTION

The study of nanostructured materials is emerging as a research area of tremendous interest, largely because of their potential functional properties in molecular recognition, chemical and biological sensors, microelectronics, optic devices, magnetic materials and catalysis^[1]. Nanoconstruction via molecular linking strategies^[1b] using metallic nanocrystal cores with organic shell encapsulation as building blocks has recently been demonstrated. Excellent examples include stepwise layer-by-layer assembling^[2-4] and DNA-based linking^[5]. Because hydrogen-bonding is one of the common non-covalent interactions in chemical and biological systems, we view it as an ideal model towards building biomimetic functional nanomaterials from the core-shell nanoparticles^[6-7]. We have recently demonstrated^[7] that hydrogen-bonding of carboxylic acid functionalized shells at gold nanocrystals of different size and shape exhibits intriguing anisotropic reactivity in terms of *cis*- or *trans*-configuration. (Scheme 1). An understanding of how structures and morphologies of such core-shell architecture correlate with size and shape has important implications to the ultimate exploration of nanostructured molecular recognition. We have employed IRS, TEM, and AFM to address relevant issues.



Scheme 1. Schematic illustration of two possible shell-shell linking via *cis*- and *trans*-configurations of the head-to-head hydrogen-bonding at carboxylic acid groups. The C_{α} - C_{β} bond is in the same side of the $C=O$ group for *cis* configuration, whereas the C_{α} - C_{β} bond is in the opposite side of the $C=O$ group for *trans* configuration.

EXPERIMENT

Synthesis. Gold nanoparticles of ~ 2 nm core size ($\text{Au}_{2\text{-nm}}$, 1.9 ± 0.7 nm) encapsulated with decanethiolate (DT) monolayer shells were synthesized by standard two-phase method [8-9]. Particles of ~ 5 nm core size ($\text{Au}_{5\text{-nm}}$, 5.2 ± 0.3 nm) were derived from the $\text{Au}_{2\text{-nm}}$ by thermally-activated processing route [10].

Preparation. As detailed in a previous report [7], DT-encapsulated $\text{Au}_{2\text{-nm}}$ and $\text{Au}_{5\text{-nm}}$ particles and COOH-terminated thiol, i.e., 11-mercaptopundecanoic acid (MUA), were used as the networking building blocks. The thin films were prepared via "exchanging-crosslinking-precipitation" route [6-7], which involved an exchange of the MUA with the gold-bound thiolates followed by crosslinking and precipitation via hydrogen bonding at the terminals. The reaction was in a toluene solvent with a controlled thiol-to-Au ratio. The thickness of the resulting thin films was controlled by immersion time.

Instrumentation. IRS spectra were acquired with a Nicolet 760 FTIR spectrometer that was purged with boil-off from liquid N_2 . It was in an external reflection mode using *p*-polarized light. A gold slide coated with octadecanethiolate- d_{37} monolayer was used as the reference. TEM was performed on Hitachi H-7000 Electron Microscope. Carbon-coated copper grid sample holder with thin films deposited on it was used for transmission measurements. AFM images were acquired using Digital Instrument's Nanoscope IIIa. The nanoparticle films were deposited on gold film on glass substrate for IRS and on glassy carbon substrate for AFM measurement.

RESULTS AND DISCUSSION

Both MUA- $\text{Au}_{5\text{-nm}}$ and MUA- $\text{Au}_{2\text{-nm}}$ films are first examined using IRS. As we have recently demonstrated [7], the carboxylic acid groups provide a diagnostic handle for probing the shell linking structure and reactivity. Figure 1 presents a set of IRS spectra for the two films (a and b). The spectrum (c) for MUA monolayer on planar gold substrate is included for comparison.

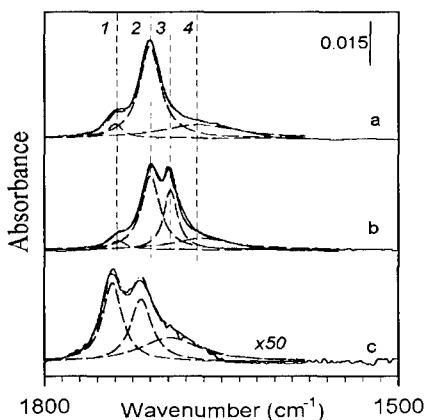


Figure 1. IRS spectra for MUA- $\text{Au}_{5\text{-nm}}$ (a), MUA- $\text{Au}_{2\text{-nm}}$ (b), and MUA monolayer (c). The dashed lines represent spectral deconvolution of the $\nu_{\text{C=O}}(\text{CO}_2\text{H})$ spectral envelope.

The $\nu(\text{COOH})$ vibration envelope in the $1740\text{--}1650\text{ cm}^{-1}$ region differ significantly between these films. The spectra of the nanoparticle films (a and b) have an overall absorbance of ~ 50 times larger than that for the monolayer (c), presumably due to a combination of the nanoparticle multilayer (~ 10 equivalent) and surface enhancement effects [6-7]. Each spectrum exhibits an envelope of multiple band components, as represented by the dashed curves based on spectral deconvolution (numerically numbered as 1, 2, 3, 4). The two nanoparticle films (a and b) show remarkable distinctions from the MUA monolayer (c) in terms of band position and relative intensity. For the MUA monolayer, the three $\nu(\text{C=O})$ bands were previously assigned [11] to $-\text{COOH}$ groups of free or non-hydrogen-bonded mode (1741 cm^{-1}), side-by-side dimeric hydrogen-bonded mode (1718 cm^{-1}), and polymeric hydrogen-bonded ($\sim 1690\text{ cm}^{-1}$) modes, respectively. In comparison, the three bands identified for the MUA- $\text{Au}_{5\text{-nm}}$ network film are displayed at 1740 cm^{-1} (1), 1710 cm^{-1} (2) and $\sim 1670\text{ cm}^{-1}$ (4). While the free acid band (1) remains basically unchanged, the shifts in the hydrogen-bonded modes (2, 4) are remarkable. We attribute these bands to the formation of head-to-head hydrogen-bonding of the $-\text{COOH}$ groups in the nanostructure. In fact, the wavenumber of band 2 is identical to the band position observed for the head-to-head hydrogen-bonding dimer with cis-configuration in condensed phases of alkanolic acids [12]. The trans-configuration is basically absent in the MUA- $\text{Au}_{5\text{-nm}}$ film. The broad band 4 is mostly due to polymeric hydrogen-bonding. Its difference from the MUA monolayer in band position reflects the difference of the hydrogen-bonding properties between head-to-head and side-by-side configurations. The head-to-head binding modes are impossible in the 2D MUA monolayers. While the 2D monolayer exhibits $\sim 40\%$ free acid component, the MUA- $\text{Au}_{5\text{-nm}}$ film shows only a level of $<10\%$. The results therefore support the formation of predominant head-to-head hydrogen-bonding linkages in the MUA- $\text{Au}_{5\text{-nm}}$ network. Interestingly, the MUA- $\text{Au}_{2\text{-nm}}$ film (b) exhibits a striking distinction from the MUA- $\text{Au}_{5\text{-nm}}$ film by displaying a new peak component at 1694 cm^{-1} (3). The relative absorbance of the free acid band ($\sim 1738\text{ cm}^{-1}$ (1)) remains a small fraction. We attribute the band at 1708 cm^{-1} (2) and the new band at $\sim 1694\text{ cm}^{-1}$ (3) to cis- and trans-modes of the head-to-head hydrogen-bonded dimers [34a] (Scheme 1), in sharp contrast to the MUA- $\text{Au}_{5\text{-nm}}$ film. It is known that the trans-configuration of alkanolic acid dimer in solids is more stable than cis-configuration [34]. The different configurations in the two films are intriguing because it demonstrates that fine structures of the hydrogen-bonding linkages are strongly dependent on particle sizes.

In the C-H region, our IRS detection of predominant methylene stretching bands at $2918\text{ \& }2848\text{ cm}^{-1}$ for the two network films further support that the network structure is primarily composed of MUA chains. The slight different from those for the MUA monolayer ($2920\text{ \& }2850\text{ cm}^{-1}$) is indicative of largely comparable chain-chain packing properties between these films. The methyl stretching bands are nearly absent for the $\text{Au}_{2\text{-nm}}$ film, consistent with a significant replacement of the original capping thiolates by MUA, which is almost 100% for the MUA- $\text{Au}_{2\text{-nm}}$ network film.

The core-shell nanocrystals and the hydrogen-bonded nanostructure are further examined using TEM and AFM to characterize their morphological properties. Figure 2 shows two representative TEM images and corresponding electron diffraction (ED) data for nanoparticles of $\text{Au}_{5\text{-nm}}$ (A) and $\text{Au}_{2\text{-nm}}$ (B) cast on carbon-coated TEM grid.

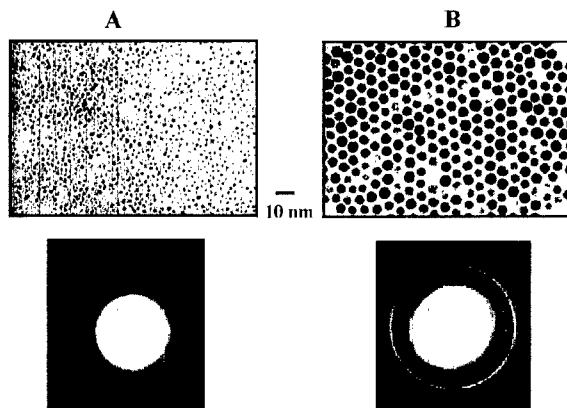


Figure 2. TEM images and corresponding ED images for Au_{5-nm} (A) and Au_{2-nm} (B).

In comparison with the two-phase synthesized nanoparticles (1.9 ± 0.7 nm, Au_{2-nm}), the thermally-processed nanoparticles (5.2 ± 0.3 nm, Au_{5-nm}) exhibit monodispersing core size and uniform shape with hexagonal outlines. These Au_{5-nm} nanocrystals also exhibit a remarkable long-range ordering feature, as reflected by the two-dimensional ordered arrays with a hexagon-type arrangement. In an agreement with the notion that the encapsulating chains are likely interdigitated between opposing alkyl shells^[1b], the determined average core-core (edge-to-edge) distance, ~ 1.5 nm, is close to the chain length expected for DT. Effects from both van der Waals attractions of the encapsulating shells and the core shape are believed to be responsible for the formation of ordered arrays. The control of nanoparticle size and shape is currently an area of great interest^[1a,10,13]. We are presently refining our thermally-activated nanoparticle processing route for processing nanoparticles towards defined size and shape. Sizes up to ~ 20 nm and shapes with triangle and rectangular features have been observed in our recent work.

The electron diffraction data (Figure 2) provide further information on the nanocrystalline properties of the two different sized particles. Crystalline features of the particles were confirmed by the ring patterns. In the ED pattern, all diffraction rings can be assigned to fcc gold. The difference in line width and intensity for all prominent diffraction lines between the two core sizes is expected based on d spacing parameters for gold and are qualitatively consistent with the dependence of electron diffraction on particle size. The relative intensities of the diffraction lines are also consistent with the results of our previous x-ray diffraction study^[10a]. The ED patterns for these two sized particles consisted of continuous rings (rather than discrete spot pattern) of the diffracted electrons because the cast particles do not have a particular orientation on the surface.

Figure 3 shows the TEM images for both MUA-Au_{5-nm} and MUA-Au_{2-nm} films. These thin films were prepared by immersing carbon film-coated TEM grids in the preparation solution for a short time (1–3 hrs) so that a monolayer or submonolayer coverage could be produced for TEM imaging.

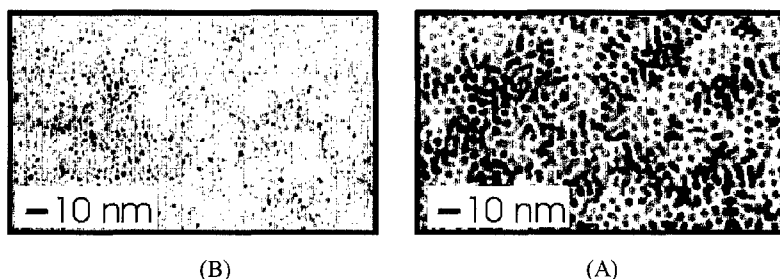


Figure 3. TEM images of submonolayer-coverage films of MUA-Au_{5-nm} (A) and MUA-Au_{2-nm} (B).

In contrast to largely evenly-spaced features observed for DT-Au nanoparticles evaporated on the grid, the images, especially for the MUA-Au_{5-nm} film (A), display regions of collectively-connected particles forming partially-continuous network, and domains including parallel lines, rings, and other type of patterns. As the film grows, these domains or patterns extend through the film. We are conducting further investigation to delineate possible chain length correlation of these features. The TEM data obtained at the submonolayer coverage provide a comparison of core-shell crosslinking or networking morphologies of the two films at the initial formation stage.

Two of the limitation of TEM imaging of the nanoparticle assembly is the special requirement of grid holder and monolayer or submonolayer coverage of the particles. AFM imaging overcomes these limitations. The capability of TappingMode(TM)-AFM allows imaging at minimum disruption of the nanostructures. A typical TM-AFM image is shown in the Figure 4 for MUA-Au_{5-nm} film assembled on a polished glassy carbon substrate. The film thickness is equivalent to 3~5 layers of nanoparticles based on an estimate from quartz-crystal microbalance data of the thin film mass loading.

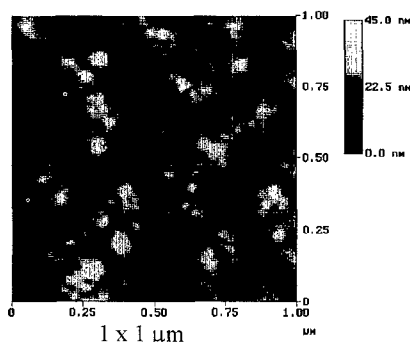


Figure 4. TM-AFM image of a MUA-Au_{5-nm} film.

The assembled nanoparticles appear to be spatially-isolated or individually-isolated. The apparent inhomogeneity feature of the overall surface morphology is probably due to the surface roughness effect of glassy carbon substrate. The particles appear somewhat larger than the core-shell particle size due to tip-sample convolution, but a cross-section view reveals an average height as expected for the particle size. Similar surface morphology has also been observed for MUA-Au_{2-nm} film.

CONCLUSION

In conclusion, the IRS results have unraveled that the molecular shell-shell linkage structure via hydrogen-bonding at carboxylic acid shell groups are dependent on the nanoparticle core size. The dependence is reflected by the detection of fine structures of cis- and trans- carboxylic hydrogen-binding linkages. The imaging studies using TEM, ED and AFM techniques have provided the morphological assessment of the core-shell nanoparticles and the hydrogen-bonding nanostructures. A further study of the fine tuning of the core-shell nanostructures is underway, which should serve as a model system of chemical manipulation at interparticle linkages for designing molecular recognition elements.

ACKNOWLEDGEMENTS

We thank Mr. H. Eichelberger for assistance in TEM measurement. The ACS Petroleum Research Fund is acknowledged for support of this research. Part of the work is also supported by NSF-CCLI Fund.

REFERENCES

1. (a) S. Link, M.A. El-Sayed, *Int. Rev. Phys. Chem.* **19**, 409 (2000). (b) A. C. Templeton, W. P. Wuelfing and R. W. Murray, *Acc. Chem. Res.* **33**, 27 (2000), and references therein. (c) C. J. Kiely, J. Fink, M. Brust, D. Bethell, and D. J. Schiffrin, *Nature* **396**, 444.(1998)
2. (a) M. Brust, D. Bethell, C. J. Kiely and D. J. Schiffrin, *Langmuir*, **14**, 5425 (1998). (b) D. Bethell, M. Brust, D. J. Schiffrin and C. J. Kiely, *J. Electroanal. Chem.* **409**, 137 (1996).
3. (a) M. D. Musick, C. D. Keating, L. A. Lyon, S. L. Botsko, D. J. Pena, W. D. Holliway, T. M. McEvoy, J. N. Richardson, and M. J. Natan, *Chem. Mater* **12**, 2869 (2000). (b) K. C. Grabar, K. R. Brown, C. D. Keating, S. J. Stranick, S. L. Tang and M. J. Natan, *Anal. Chem.* **69**, 471 (1997).
4. (a) F. P. Zamborini, J. F. Hicks and R. M. Murray, *J. Am. Chem. Soc.* **122**, 4514 (2000). (b) A. N. Shipway, M. Lahav, R. Blonder and I. Willner, *Chem. Mater.* **11**, 13.(1999).
5. C. Mirkin, R. L. Letsinger, R. C. Mucic and J. J. Storhoff, *Nature*, **382**, 607 (1996).
6. F.L Leibowitz, W. X. Zheng, M. M. Maye and C. J. Zhong, *Anal. Chem.* **71**, 5076 (1999).
7. W.X. Zheng, M.M. Maye, F.L. Leibowitz and C.J. Zhong, *Anal. Chem.* **72**, 2190 (2000).
8. M. Brust, M. Walker, D. Bethell, D. J. Schiffrin and R. Whyman, *J. Chem. Soc., Chem. Commun.*, 801 (1994).
9. M. J. Hoetjeter, J. E. Wingate, C. J. Zhong, J. E. Harris, R. W. Vachet, M. R. Clark, J. D. Londono, S. J. Green, J. J. Stokes, G. D. Wignall, G. L. Glish, M. D. Porter, N. D. Evans and R. W. Murray, *Langmuir* **14**, 17 (1998).
10. (a) M. M. Maye, W. X. Zheng, F. L. Leibowitz, N. K. Ly and C. J. Zhong, *Langmuir* **16**, 490 (2000). (b) M. M. Maye and C. J. Zhong, *J. Mater. Chem.* **10**, 1895 (2000).
11. Y.-T. Tao, W.-L. Lin, G. D. Hietpas and D. L. Allara, *J. Phys. Chem. B* **101**, 9732 (1997).
12. S. Hayashi and J. Umemura, *J. Chem. Phys.* **63**, 1732 (1975).
13. R. L. Whetten, J. T. Khoury, M. M. Alvarez, S. Murthy, L. Vezmar, Z. L. Wang, P. W. Stephens, C. L. Cleveland, W. D. Luedtke and U. Landman, *Adv. Mater.* **8**, 428 (1996).